CALCULATIONS OF THREE-DIMENSIONAL HYPERVELOCITY CONE-FLOW WITH CHEMICAL REACTIONS

M.N. MACROSSAN, D.I. PULLIN and N.J. RICHTER

Department of Mechanical Engineering
University of Queensland, St. Lucia, Qld. 4067
AUSTRALIA

ABSTRACT

We discuss calculations using the equilibrium flux method, for the hypervelocity flow of nitrogen with dissociation/recombination chemical reactions about a slightly blunted cone at incidence. Test results for frozen flow are compared with the cone flow results of Marconi (1989). Specific examples using the Lighthill-Freeman model of the ideal dissociating gas show substantial interaction between gas dynamics and chemistry on the leeward cone surface.

1. INTRODUCTION

A good understanding of the interaction between real gas nonequilibrium chemistry and three-dimensional hypervelocity aerodynamics may be important in the design of single-stage-to-orbit (SSO) space vehicles. During ascent to orbit real-gas effects should be confined to stagnation zones and to the internal flow in scramjet-type power plants. Reentry to the atmosphere of a slender SSO vehicle at hypervelocity speeds will produce sustained periods of flight with chemical reactions in the external flow behind the body shock wave, and these in turn will interact with aerodynamic phenomena including shock induced separation and transition to turbulence in the boundary layer. Such effects are little understood.

Numerical prediction of real-gas hypervelocity leeward flows is likely to be very difficult and will clearly require progress in the development of both Euler and Navier-Stokes codes coupled to a realistic chemistry model for reactive air. In this paper, as a first step, we describe an application of the Equilibrium Flux Method (EFM Pullin 1980) to the numerical simulation of the Euler equations for three-dimensional hypervelocity flow of nitrogen about cone-shaped bodies at incidence. The only chemical reactions present are the dissociation and recombination reactions

$$N_2 + M \Longleftrightarrow 2N + M ,$$

where the collision partner $M = N$ or N_2. These reactions give a good qualitative description of the real gas behaviour of air. We use the Lighthill-Freeman (Freeman 1958) ideal dissociating gas (IDG) model to represent nitrogen. Non-equilibrium reacting flows and perfect gas (frozen chemistry) flows are considered. The computations are complementary to experiments on hypervelocity flow past bodies of revolution at incidence being performed in the T4 shock tunnel at the University of Queensland (Krek et al, 1989). Ultimately we plan to match the free-stream conditions for the computations to those produced in the test section of the shock tunnel. Our present aim is to test the numerical method against known results for frozen flow and to describe some preliminary results, with near experimental free-stream conditions, in order to illustrate the effects of non-equilibrium chemistry on the flow.

2. THE EQUILIBRIUM FLUX METHOD (EFM)

EFM may be interpreted as the infinite collision rate limit of the Monte-Carlo Direct Simulation Method (Bird 1976) for rarefied gas dynamics. It is a finite-volume shock-capturing method and, since it is naturally flux-splitting (Deshpande 1986), it is automatically upwinding. EFM has none of the stability problems encountered by many numerical methods when applied to mixed subsonic-supersonic flows. Here we give a brief description of EFM; detailed descriptions are given by Pullin (1980) and Macrossan (1989). EFM may be obtained from the Boltzmann equation (see Bird 1976),

$$\frac{\partial}{\partial t}(nf) + c.\nabla(nf) = [\partial(nf)/\partial t]_{coll} , \qquad (1)$$

where n is the number density, $c = (c_x, c_y, c_z)$ is the molecular velocity, f is the velocity distribution function and the RHS represents the collision integral.

Now consider a volume V of (x,y,z) space divided into N contiguous cells of volume V_i for i = 1,N. Let S be the surface of V_i and $\hat{n}$ the outward normal. Conservation equations for the continuum properties of mass, momentum and energy can be obtained by first multiplying (1) by the corresponding molecular quantity $Q = [m, mc, m(1/2\ c^2 + e_{st})]$, where m is the molecular mass and e_{st} is the specific energy in the molecular structure (including chemical energy), and then integrating over V_i and over all velocities. Applying Gauss's theorem to the second volume integral and noting that $\int_{-\infty}^{\infty} Q\ [\partial(nf)\partial t]_{coll} dc = 0$ then gives

$$\frac{\partial}{\partial t} \int_{V_1} \overline{nQ}\ dV + \int_S \langle nQc \rangle\ dS = 0 , \qquad (2)$$

where

$$\overline{nQ} = \int_{-\infty}^{\infty} nQf\ dc , \qquad \langle nQc \rangle = \int_{-\infty}^{\infty} nQf c.\hat{n}\ dc, \qquad (3)$$

with $dc = dc_x dc_y dc_z$. The components of $\overline{nQ}$ are $[\rho, \rho v, \rho(1/2v^2 + e_{int})]$ where ρ is the fluid density, $v = \bar{c}$ is the velocity and e_{int} is the specific internal energy.

EFM proceeds by integrating (2-3) forward in time t under the assumption that nf is given by the local Maxwellian distribution

$$nf_0 = n\beta^3\ exp[-\beta^2(c-v)^2]/\pi^{3/2}, \qquad (4)$$

where $\beta = (2RT)^{-\frac{1}{2}}$, T is the temperature and R is the ordinary gas constant. In first-order EFM it is assumed that all gas properties are constant across each cell and are discontinuous at the interfaces between the cells. Let + and − refer to the interior and exterior of V_i respectively. Then $\langle nQc \rangle$ in (3) may be split as

$$\langle nQc \rangle = \int^+ nQf_0^+\ c.\hat{n}\ dc + \int^- nQf_0^-\ c.\hat{n}\ dc , \qquad (5)$$

where $\int^+$ and $\int^-$ denote integration over outward moving $(c.\hat{n} > 0)$ and inward moving $(c.\hat{n} < 0)$ particles respectively. Now if at time t all gas properties in cells are known then f_0^+ and f_0^- are known and (5) can be

evaluated analytically. Putting Q = m, for example, gives the outward and inward directed mass fluxes as

$$\langle \rho c \rangle^\pm = \frac{\rho^\pm}{\beta^\pm} [\exp(-s^{\pm 2}) + \pi^{1/2} s^\pm H(s^\pm)] /(2\pi^{1/2}) , \quad (6)$$

where $s^\pm = \pm c^\pm . \hat{n}$ $\beta^\pm$ are the outward and inward components of the normal speed ratio, $H(s) = 1 + \text{erf}(s)$ and erf is the error function. The net mass flux across dS is $\langle \rho c \rangle^+ - \langle \rho c \rangle^-$. Similar expressions are obtained for the other components of $\langle nQc \rangle$. At the end of each time step Δt new gas properties are calculated from the totals of nQ in each cell and the known cell volumes.

The chemical reactions are de-coupled from the gas dynamics over Δt. First the reactions are assumed to be frozen and the fluxes between cells are computed using the gas constant and e_{st} for the local (frozen) chemical composition. Before the fluxes in the next Δt are calculated, an adiabatic chemical reaction in each cell is advanced for Δt at a rate appropriate to the local density and temperature. The chemical composition and the temperature, but no other fluid properties, are changed by the reaction.

The law of mass action for the ideal dissociating gas (Lighthill 1957) is

$$\alpha^2/(1 - \alpha) = \rho_d/\rho \exp(-\theta_d/T) , \quad (7)$$

where $\alpha = [N]/([N] + 2[N_2])$ is the mass fraction of dissociated nitrogen, $\theta_d = 113,200$ K and $\rho_d = 130$ gm/cc. The equation of state for the reacting mixture and the ratio of specific heats γ are given by

$$p = \rho (1 + \alpha) R_{nn} T , \qquad \gamma = (4 + \alpha)/3, \quad (8)$$

respectively, where p is pressure and R_{nn} is the ordinary gas constant for N_2. The IDG model is a good representation of N_2 for $T > 2000$ K and for $\alpha > 0.05$, conditions which are to be expected in hypervelocity flight.

Following Freeman (1958), the chemical rate equation for IDG can be written as

$$d\alpha/dt = \rho X(\alpha,T) [(1 - \alpha) \exp(-\theta_d/T) - \rho\alpha^2/\rho_d] , \quad (9a)$$

where

$$X(\alpha,T) = [C_1 T^{\eta_1}\alpha + 2 C_2 T^{\eta_2}(1 - \alpha)]/W , \quad (9b)$$

and W is the molecular weight of N_2. We have taken the values of $C_1 = 8.5 \times 10^{25}$, $C_2 = 2.3 \times 10^{29}$ (cgs units), $\eta_1 = -2.5$ and $\eta_2 = -3.5$ (Kewley and Hornung 1974).

In the present calculations Δt was such that the CFL number in any cell was less than 1 and much smaller than the characteristic reaction time $(d\alpha/dt)^{-1}$ in each cell. Consequently a simple Euler method was used to advance the chemical reactions.

3. FREE-STREAM CONDITIONS AND BODY GEOMETRY

The free-stream conditions, cone semi-angle δ and angle of attack θ for the four calculations discussed presently are summarized in table 1. Case 1 was used to test the code against the accurate cone-flow calculations of Marconi (1989). Cases 2-4 have the same geometry and similar free-stream conditions but chemistry is active only in cases 3-4. The free stream velocity U lies in the x-y plane at an angle θ to the positive x-axis which is coincident with the body axis. The body had a small blunted nose in the form of a cubic of revolution beginning at x = 0 and which joined smoothly onto the cone at x = .05L, where L is the body length. Because of symmetry only one half of the flow (z > 0) need be considered.

Two computational grids were used. Grid 1 surrounded the body nose and consisted of $N_1 \times N_2 \times N_3 = 3 \times 25 \times 50$ cells, where N_1, N_2 and N_3 are the cell numbers along the body generator, normal to the body generator and

Case	M	δ	θ	γ	Chemistry
1	5	10	20	1.4	frozen
2	6	15	30	1.4	frozen
3	6	15	30	1.4	finite rate
	U = 6km/s			ρ = 6x10^{-2}kg/m^3	
	α = 0.2	T = 2000 K		L = 1m	
4	6	15	30	1.4	finite rate
	as for case 3 but			ρ = 2x10^{-2}kg/m^3	

TABLE 1. Freestream conditions

azimuthally between the windward and leeward flow planes respectively. Grid 2 started at the downstream end of grid 1 and contained 22x50x100 cells.

Different modes of EFM were used on grids 1 and 2. On grid 1 a "time marching" mode was used in which the conservation equations were integrated simultaneously in all cells, starting from impulsive initial conditions, until steady state was reached. This was necessary because there is a small region of subsonic flow near the body nose. On grid 2 a space marching mode was used, in which steady state was found on successive slices of the grid approximately parallel to the y-z plane. This can only be successful if the flow on grid 2 is always supersonic. For both modes the CFL number was near 0.5.

4. HYPERVELOCITY CONE FLOW

The general structure of hypersonic cone-flow at incidence has been demonstrated by the cone-flow calculations of Marconi (1989). These results show that with frozen chemistry (i.e. γ constant), the flow is conical. A bow shock is followed by weakly rotational flow in the shock layer adjacent to the windward cone surface. The gas expands rapidly on the leeward surface but undergoes recompression when approaching the leeward plane of symmetry. For sufficiently large angle of attack at hypersonic Mach number this produces a pair of cross-flow shocks and the resulting large entropy gradient along the leeward side of these shocks generates a complex flow structure containing one or more pairs of compact vortices coupled with separated flow from the cone surface. Marconi shows that this structure is essentially inviscid although it will be modified by the presence of the cone boundary layer which will contribute to the post-shock vorticity field via shock-induced separation.

Figure 1 shows the surface pressure for case 1 plotted as $\ln(p/p_0)$ at x/L = 0.852 versus azimuthal angle ϕ measured from the windward ray of symmetry, compared with Marconi's results for pure cone flow. There is good agreement on the windward surface, where the surface pressure is dominated by the free-stream dynamic pressure, and the position of the leeward cross-flow shock is accurately captured by the present computations. On the leeward side of the cross-flow shocks Marconi finds various spiral vortex structures depending on θ, δ and M. For case 1 our calculations do not reproduce this structure in detail. Marconi's shock-fitting numerical method is of high order spatially but is implemented for strictly cone flow. The EFM technique is robust geometrically and can easily accommodate chemical reactions but is presently implemented in only first-order spatially accurate form. This may account for the discrepancies of figure 1. A second or higher spatial-order EFM will be required to resolve flow details behind the leeward shock.

Figures 3-7 show perspective views of four surfaces of grid 2 : the plane of symmetry (x-y plane) comprising the windward (lower, ϕ = 0) and leeward (upper, ϕ = 180°) portions ; the cone surface ; and a curved surface in the flow locally normal to the cone surface and located near the downstream end of grid 2. The viewpoint is upstream of the body, somewhat above the

x-z plane. Figures 3-4 and 6-7 show contours of various flow quantities on the four surfaces. Figure 5 depicts three-dimensional velocity vectors at a subset of cell centres on the four surfaces for case 4, table 1. The bow and leeward shocks are clearly visible and the curved particle paths at the cone surface can be inferred.

In figure 3 we show contours of α for the chemically active flow of case 4. In order to test the first-order effects of chemistry for the cone-flow, the parameters for cases 3-4 were chosen to match geometry, γ and, as near as possible, M to the frozen flow of case 2. Consequently, with $\alpha = 0.2$ the freestream is not in local chemical equilibrium, and some recombination occurs before the flow encounters the bow shock wave. This can be seen in figure 3 and also in the contour plot of $\ln(T/T_0)$ in figure 7 (T_0 is the initial free stream temperature), where the temperature rises upstream of the bow shock owing to energy released in the recombination reaction.

The variation of α in the flow is perhaps best evaluated by comparing figure 3 with the contours of $\alpha_{eq}-\alpha$, shown for $\alpha_{eq}-\alpha < 0$ in figure 4. We define α_{eq} as a local adiabatic equilibrium value of the dissociation fraction, calculated from the local flow state assuming equilibrium with no change in specific internal energy. Note from figure 4 that $\alpha_{eq}-\alpha$ is negative over most of the flow, indicating that recombination is the locally dominant reaction. Together figures 3-4 indicate that, following the rapid gas temperature rise through the bow shock (see figure 7), $\alpha_{eq}-\alpha$ is positive and that consequently the flow begins to dissociate strongly just downstream of the shock. Dissociation appears to be confined to a thin region near the shock and also adjacent to the windward plane of symmetry. Fluid processed by the shock very near $\phi = 0^0$, and which remains near the windward symmetry plane until well downstream (see figure 5) thus becomes frozen or quenched (Stalker 1989) in a dissociated state. Away from $\phi = 0^0$ the temperature falls quickly as dissociation soaks up thermal energy and the density rises. Recombination then nearly equals dissociation, which decreases rapidly as T decreases and the flow approaches local chemical equilibrium.

As the flow approaches the leeward surface $\phi > 90^0$, T is falling and dissociation stops owing to the $\exp(-\theta_d/T)$ effect (see eq (9a)), but recombination continues. Since the recombination rate is proportional to ρ^2, however, and since ρ falls rapidly in the leeward flow, recombination is insufficient to bring the flow to local equilibrium. The leeward flow then becomes nearly frozen, the mechanism being similar to that which gives chemical freezing in rapidly expanding nozzle flows. Note that figure 3 shows α not constant along rays from the cone nose, and so in this respect the flow is far from conical.

When the flow is processed by the leeward shock, ρ increases and recombination increases. This moves the gas toward equilibrium as can be seen from figure 4, which shows $|\alpha_{eq}-\alpha|$ decreasing behind the leeward shock.

Finally we note that active chemistry appears to influence the position of the leeward shock. This is evident from a comparison of the temperature fields in figures 6 and 7, and also from the surface pressure plots in figure 2.

5. CONCLUSIONS

Our results show that the equilibrium flux method for simulation of the Euler equations can be adapted to 3-D gas flows with dissociation/recombination chemical reactions. Improvements in EFM currently under development include : (1) Implementation of a second order scheme for the flux calculation which accounts for gradients of flow properties across cells. First order EFM has numerical viscosity proportional to cell dimension (Macrossan 1989), whereas a second order scheme may be expected to change this dependence to order the square of the cell dimension. (2) Inclusion of viscous shear stresses in the flux equations. This is only feasible for a second or higher order method. (3) Implementation of a realistic multiple species/reaction model for air.

In future work we will attempt to assess real gas effects for flows achievable in the T4 wind tunnel, and to relate experimental results to those for an equilibrium freestream at true hypervelocity flight conditions. We also plan to investigate possible scaling laws through parametric studies.

REFERENCES

Bird, G.A. 1976, *Molecular Gas Dynamics*, OUP.
Deshpande, S.M. 1986, *AIAA* paper 86-0275.
Freeman, N.C. 1958, *J. Fluid Mech.*, **4**, 407.
Lighthill, M.J. 1957, *J. Fluid Mech.*, **2**, 1.
Kewley, D.J and Hornung, H.G. 1974,
    Chem. Phys. Letters, **25**, 531.
Krek, R., Hannerman, K., and Pullin, D.I. 1989,
    Submitted to *10AFMC*.
Macrossan, M.N. 1989, *J. Comp. Phys.* **80**, 204.
Marconi, F. 1989, *Comput. Fluids*, **17**, 151.
Pullin, D.I. 1980, *J. Comp. Phys.* **34**, 231.
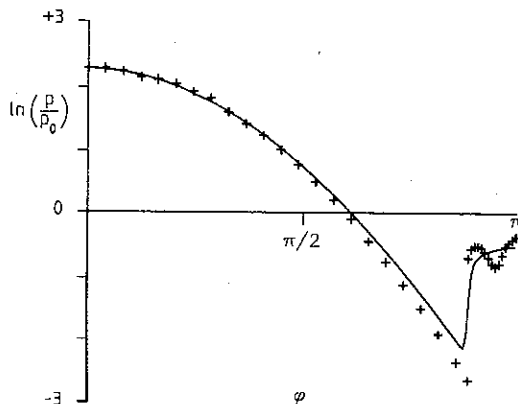Stalker, R.J. 1989, *Ann. Rev. Fluid Mech.* **21**, 37.

Figure 1. Cone surface pressure at constant x plotted as $\ln(p/p_0)$ versus azimuthal angle ϕ, where p_0 is the freestream pressure. Case 1. ——————— present calculation, $x/L = 0.852$. + Marconi (1989).
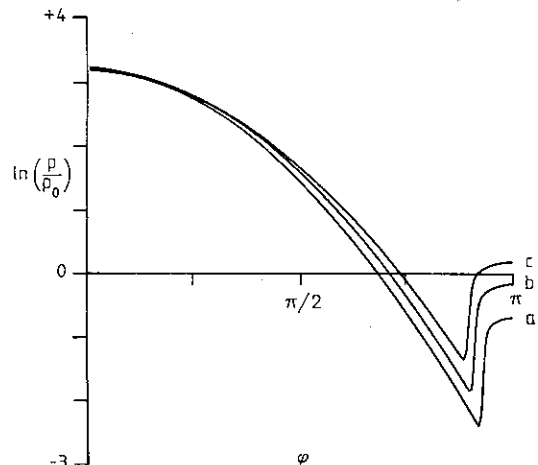

Figure 2. Cone surface pressure $\ln(p/p_0)$ versus ϕ. Key a: case 2 (frozen flow), b : case 4, c : case 3 – This flow is near chemical equilibrium.
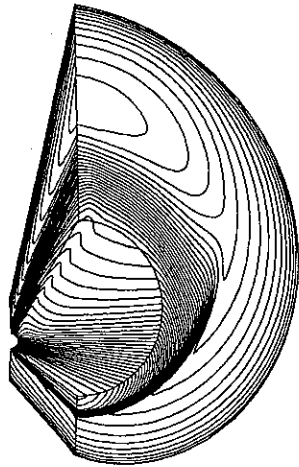
Figure 3. Perspective view of contours of α, on four surfaces within grid 2 : windward and leeward planes ; cone surface ; a curved slice locally normal to cone surface at x/L = 0.852. Case 4, range: $0.14 < \alpha < 0.35$.
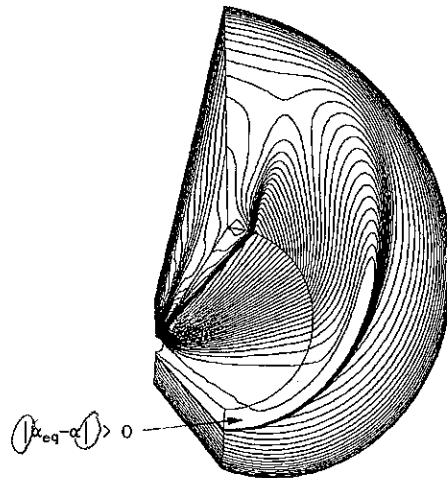

Figure 4. Perspective view of contours of $\alpha_{eq}-\alpha$ on four surfaces within grid 2. Only $\alpha_{eq}-\alpha$ negative depicted. Case 4. Range : $-0.095 < \alpha_{eq}-\alpha \le 0$. Full range in calculation : $-0.095 < \alpha_{eq}-\alpha < .0.065$.
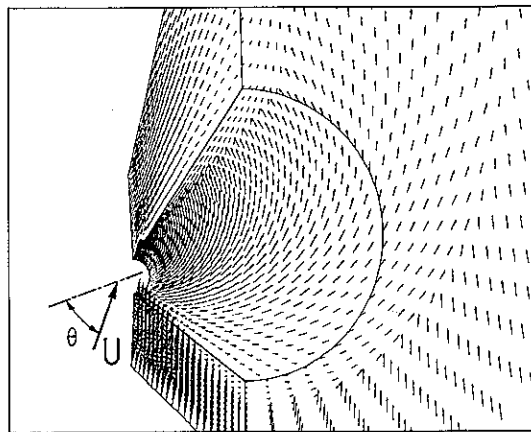

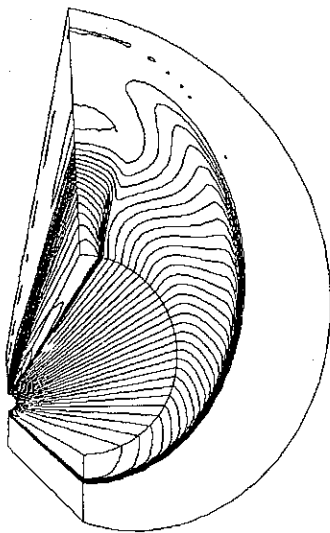Figure 5. Perspective view of velocity vectors on four surfaces of grid 2. Case 4.

Figure 6. Perspective view of contours of $\ln(T/T_0)$ on four surfaces within grid 2. Case 2 : frozen flow. Range : $-0.05 < \ln(T/T_0) < 1.75$
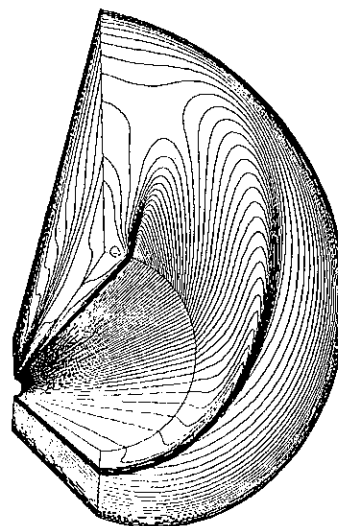

Figure 7. Perspective view of contours of $\ln(T/T_0)$ on four surfaces within grid 2. Case 4. Range $0 \le \ln(T/T_0) < 1.55$

12.36